Plasma Sources Sci. Technol. **18** (2009) 034022 (12pp) doi:10.1088/0963-0252/18/3/034022

Ion diagnostics of a discharge in crossed electric and magnetic fields for electric propulsion

S Mazouffre[1], V Kulaev[1] and J Pérez Luna[2]

[1] ICARE, CNRS, 1C avenue de la Recherche Scientifique, 45071 Orléans, France
[2] LAPLACE, CNRS, University of Toulouse, 118 route de Narbonne, 31062 Toulouse, France

E-mail: stephane.mazouffre@cnrs-oleans.fr

Received 28 June 2008, in final form 3 March 2009
Published 15 July 2009
Online at stacks.iop.org/PSST/18/034022

Abstract

The velocity distribution function (VDF) of metastable Xe^+ ions was measured along the channel centerline of the high-power PPS®X000 Hall effect thruster by means of laser induced fluorescence (LIF) spectroscopy at 834.72 nm for various discharge voltages (300–700 V) and propellant mass flow rates (6–15 mg s^{-1}). The development of the on-axis profile of the velocity dispersion reveals the interrelation between ionization and acceleration layers. The ion velocity profiles are in accordance with outcomes of a hybrid numerical model in which the electron mobility is assessed from particle-in-cell simulations. The axial distribution of the effective electric field is inferred from the mean ion velocity profile, despite the parasitic effect due to ions created in the acceleration region. Most of the acceleration process takes place outside the thruster channel. The electric field augments and it moves upstream when the applied voltage is ramped up. The impact of the xenon mass flow rates is found to depend upon the voltage. A novel approach based on the moments of the experimental VDFs in combination with the Boltzmann's equation is introduced in order to determine the real electric field distribution. The method also provides the ionization frequency profile. The LIF diagnostics reveals the existence at the end of the acceleration region of fast ions of which the kinetic energy is above the supplied energy. The fraction of these supra-sped up ions grows when the voltage increases. The ion VDFs were also recorded in the plasma plume far field by way of a retarding potential analyzer (RPA). The shape of the RPA traces as well as their evolution with operating conditions are in agreement with trends observed by means of LIF spectroscopy. Finally, physical mechanisms at the origin of supra-sped up ions are discussed in light of numerical simulation outcomes and a set of new experimental results.

(Some figures in this article are in colour only in the electronic version)

1. Introduction

Electric propulsion is nowadays a well-established technology for space applications [1]. Among all proposed electric propulsive devices, Hall effect thrusters (HETs) are currently recognized as an attractive propulsion means for long duration missions and for maneuvers that require a large velocity increment. HETs, also called closed electron drift thrusters, are advanced propulsion devices that use an electric discharge with magnetized electrons to ionize and accelerate a propellant gas [2]. Due to interesting features in terms of propellant ejection speed, efficiency, flexibility and lifetime, HETs are employed for missions like geo-stationary satellite orbit correction and station keeping. New fields of application are nowadays envisaged for electric propulsion systems. Low power Hall thrusters (∼100 W) seem suited for drag compensation of observation satellites that operate on a low-altitude orbit in the Earth's atmosphere. The use of high-power (∼5 kW) Hall thrusters for orbit raising and orbit topping maneuvers of communication satellites would offer

 © 2009 IOP Publishing Ltd Printed in the UK

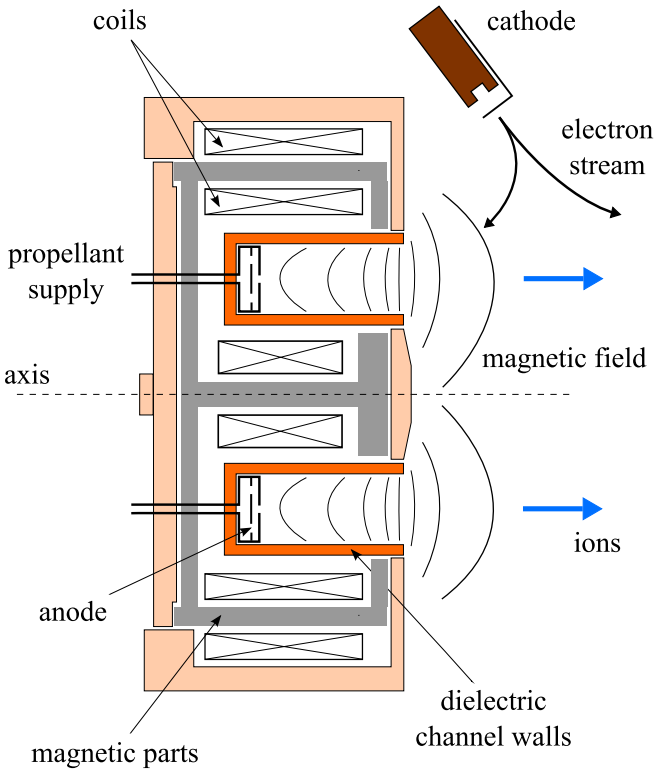

Figure 1. Cross-section view of a HET.

significant benefits in terms of launch mass, payload mass and operational life. In addition, 5–10 kW-class HETs appear as good candidates to be used as the primary propulsion engine for robotic space probes during interplanetary journeys towards far-off planets and asteroids.

A schematic of a HET is depicted in figure 1. The basic physics of a HET implies a magnetic barrier and a low pressure dc discharge generated between an external hollow cathode and an anode in such a way that a crossed electric and magnetic fields discharge is created [2–4]. The anode, which also serves as gas injector, is located at the upstream end of a coaxial annular dielectric channel that confines the discharge. Xenon is generally used as a propellant gas for its specific properties in terms of high atomic mass and low ionization energy. A set of solenoids provides a radially directed magnetic field $\boldsymbol{B}$ of which the strength is maximum in the vicinity of the channel exhaust. The magnetic field is chosen strong enough to make the electron Larmor radius much smaller than the channel characteristic sizes, but weak enough not to affect ion trajectories. High-energy electron trapped inside the channel are responsible for the efficient ionization of the supplied gas. The electric potential drop is mostly concentrated in the final section of the channel owing to the low electron axial mobility in this restricted area. The corresponding induced local axial electric field $\boldsymbol{E}$ has two main effects. First, it drives a large electron azimuthal drift: the Hall current. Second, it accelerates ions out of the channel, which generates thrust. The ion beam is neutralized by a fraction of electrons emitted from the hollow cathode. When operating near 1.5 kW, a HET ejects ions at 20 km s^{-1} and generates 100 mN of thrust with an overall efficiency of about 50%.

Several physical mechanisms that govern the behavior of the low-pressure $\boldsymbol{E} \times \boldsymbol{B}$ discharge of a HET are still ill-understood. Among others one can cite anomalous electron diffusion across the magnetic barrier [5–7], plasma–wall interactions [8, 9], interrelation between ionization and acceleration processes [10] as well as energy losses [11]. This lack of knowledge is a limiting factor in optimizing existing HETs over a broad range of input power, to define novel and more efficient thruster geometry and structure, and to develop predictive numerical modeling tools. As we will see, the fine examination of ion transport phenomena in a HET is a powerful way to improve our understanding about the physics at work in this specific type of plasma source. As Xe^+ ions are not magnetized, by measuring the ion velocity it is possible to reconstruct the electric field distribution, the latter being linked to the magnetic field map and the anomalous electron diffusion. A measurement of the ion velocity spread provides valuable information about the interrelation between the ionization and the acceleration processes and the link between thrust and specific impulse generation. The observation of fast ions of which the kinetic energy is higher than the applied potential energy is a relevant feature of a HET plasma that reveals a peculiar dynamics of the electric field. Besides, the ion velocity distribution function (VDF) is a local statistical quantity that can directly be compared with outcomes of kinetic and hybrid computer simulations.

Near-infrared laser induced fluorescence (LIF) spectroscopy has often been used in the past few years to measure the velocity of metastable ions in the plasma of a Hall thruster [10, 12–15]. In this contribution, we present spatially resolved measurements of the temporally averaged Xe^+ ion VDF in the discharge chamber and in the plasma plume of the 5 kW-class PPS®X000 HET performed by means of continuous-wave LIF spectroscopy. Ion VDFs were measured parallel to the thruster axis, i.e. in the ion flow direction, for a broad range of discharge voltages 300–700 V and propellant mass flow rates 6–15 mg s^{-1}. On-axis profiles of the time-averaged ion axial velocity and velocity dispersion deliver interesting information about ionization and acceleration processes and their interrelation, in agreement with outcomes of hybrid and kinetic modeling approaches. An accurate extraction of the electric field distribution, an essential quantity, from the measured ion velocity is always difficult. In contrast to previous studies [10, 15–17], the electric field is not directly inferred from the ion velocity profile. Here, the electric field is obtained by using a novel method based on the moments of the ion VDFs, which permits one to withdraw parasitic effects. The ion VDF were also probed in the thruster far field by means of a retarding potential analyzer (RPA). The shape of the distribution functions recorded by RPA as well as evolution with operating conditions are in agreement with trends observed by way of LIF spectroscopy. Finally, physical mechanisms at the origin of very fast ions of which the kinetic energy is above the supplied energy are discussed in light of numerical simulation outcomes and new experimental facts.

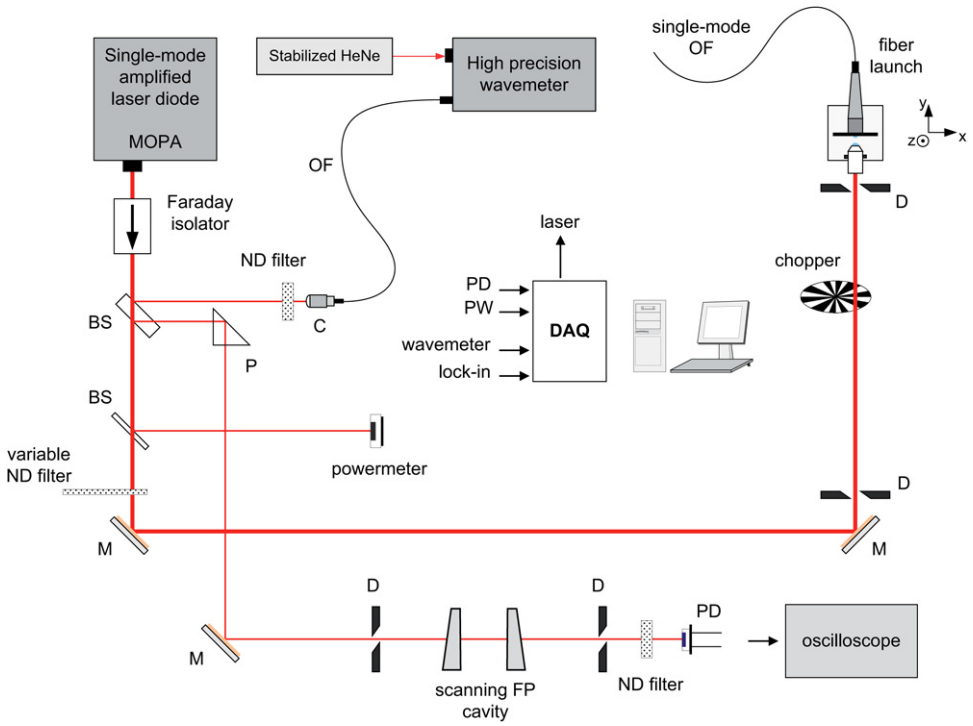

Figure 2. Schematic of the continuous-wave LIF optical bench.

2. LIF diagnostics

2.1. Method and experimental arrangement

The LIF spectroscopy is a non-intrusive diagnostic tool that enables one to determine the velocity of probed particles along the laser beam direction by measuring the Doppler shift of absorbed photons [18]. The transition used in this study is the $5d\,^2F_{7/2} \rightarrow 6p\,^2D^o_{5/2}$ at $\lambda_{air} = 834.7233$ nm, which has been chosen due to a large population in the $5d\,^2F_{7/2}$ metastable state of Xe^+ ion and due to the favorable branching ratio of the $\lambda_{air} = 541.915$ nm line originating from its upper state, which allows non-resonant LIF. Measuring the frequency ν at which the laser beam energy is absorbed permits one to determine the ion Doppler shift and subsequently the ion velocity component corresponding to the laser beam direction.

The LIF optical bench is extensively described in [10, 15]; however, in this work changes were made in order to accurately control the laser beam profile. The laser beam used to excite Xe^+ metastable ions is produced by an amplified tunable single-mode external cavity laser diode (MOPA) that can deliver up to 700 mW of power in the near-IR spectral domain. The laser remains mode-hop free over a frequency tuning range of more than 10 GHz. The spectral width of the laser beam profile is about 1 MHz. Behind the tapered amplifier the laser beam passes through a Faraday isolator to prevent optical feedback into the laser cavity. The wavelength is accurately measured by means of a calibrated wavemeter whose absolute accuracy is better than 100 MHz, which corresponds to 90 m s^{-1}. A plane scanning Fabry–Pérot interferometer with a 1.29 GHz free spectral range is used to real-time check the quality of the laser mode and to detect mode hops. The power of the beam is also continuously monitored. The primary laser beam is modulated by a mechanical chopper at a frequency ∼1 kHz before being coupled into a 50 m long single-mode optical fiber of 5 μm core diameter. The fiber allows the beam to be carried into the vacuum chamber of the PIVOINE-2g ground-test facility. A schematic of the optical bench is shown in figure 2. The fiber output is located behind the thruster. Collimation optics are used to form a narrow beam that passes through a hole 2.2 mm in diameter located at the back of the PPS®X000 thruster. The laser beam propagates along the channel centerline in the direction of the ion flow. Power deposition in the measurement volume is well controlled as the laser beam spatial profile is composed solely of one symmetric mode. Typically, the laser power density reaches 3 mW mm^{-2}, which warrants a weak saturation effect on the studied transition.

A detection branch made of a 40 mm focal length, which focuses the fluorescence light onto a 200 μm core diameter optical fiber, is mounted onto a travel stage perpendicular to the channel axis. The magnification ratio is 1, meaning that the spatial resolution is 200 μm in the axial direction. A slit 16 mm in length was made in the channel dielectric outer wall in order to carry out measurements inside the channel. The collection system allows one to probe an area stretching from 16 mm into the channel up to 50 mm outside. The measurement configuration and the coordinate system are shown in figure 3. The LIF light transported by the 200 μm fiber is focused onto the entrance slit of a 20 cm focal length monochromator that isolates the 541.9 nm line from the rest of the spectrum. A photomultiplier tube serves as a light detector. A lock-in amplifier operating at the chopper frequency is used to discriminate the fluorescence light from the intrinsic plasma emission. Scanning of the MOPA cavity, data acquisition and laser wavelength monitoring are computer controlled.

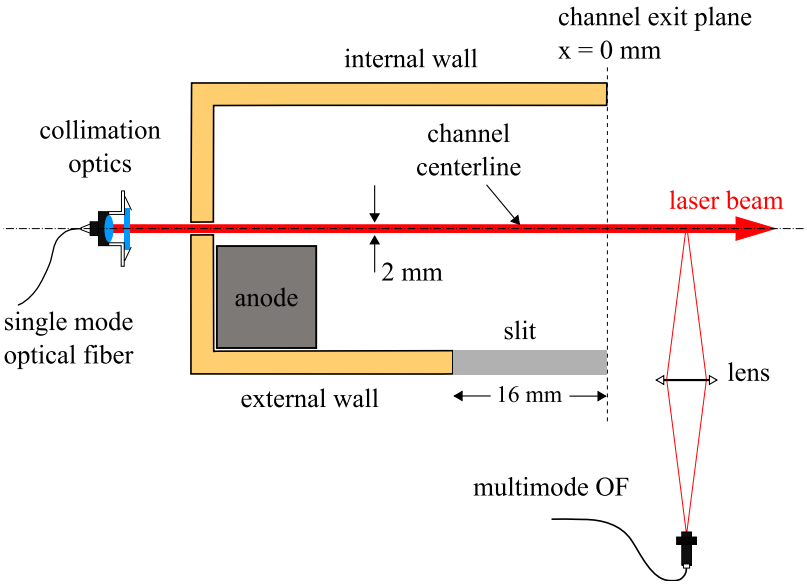

Figure 3. Schematic of the LIF measurement configuration. The laser beam shines along the channel centerline. The axial coordinate x is the distance from the channel exit plane. It is defined as positive along the thrust vector.

2.2. Thruster operating conditions

All measurements were performed in the PIVOINE-2g ground-test facility. The PPS®X000 thruster was equipped with BN–SiO_2 dielectric channel walls and a carbon anode. The channel is around 30 mm in length. The magnetic field is maximum at the channel exit with $B \sim 150$ G. During the experiments campaign, the applied voltage U_d and the anode xenon mass flow rate Φ_a have been changed:

- Voltage series ($\Phi_a = 6$ mg s^{-1}): $U_d = 300$, 400, 500, 600 and 700 V.
- Mass flow rate series ($U_d = 300$ V): $\Phi_a = 6$, 10 and 15 mg s^{-1}.

The xenon gas flow rate through the cathode was kept fixed at 0.6 mg s^{-1} and the magnetic field was unchanged. The power range stretched from 1500 to 4500 W. The background pressure inside the vacuum chamber was $\sim 1.4 \times 10^{-3}$ Pa-Xe for all conditions but at 15 mg s^{-1}. In that case the pressure was 2×10^{-3} Pa-Xe. The impact of magnetic field strength on the ion velocity was investigated in previous works [10, 15]. Data points at 300 and 400 V with $\Phi_a = 6$ mg s^{-1} are taken from a preceding study [15]. In the range 500–700 V, results were obtained by means of the optimized optical bench hereinbefore described; they offer a higher signal-to-noise ratio (SNR) that allows one to draw more stringent conclusions.

2.3. Velocity distribution functions

The width of a recorded fluorescence profile is typically around 3000 m s^{-1} ($\Delta\nu \approx 3.5$ GHz) in the region of a strong magnetic field as can be seen in figure 4. There exits 9 stable isotopes of xenon, two of which have a non-zero nuclear spin. As a consequence the studied transition is made of 19 components. The most intense components form a distribution whose width is around 620 m s^{-1} (740 MHz) at 900 K. The hyperfine and isotopic structure can then be neglected. In addition, the velocity dispersion due to the electrostatic acceleration of various isotopes is small with respect to the observed line width. One finds $\Delta v \approx 870$ m s^{-1} at 700 V in the case of xenon. This effect, however, contributes to the width of the profile behind the acceleration region. Due to the thruster magnetic field, the optical transition experiences the Zeeman effect, which leads to a splitting of all levels into manifold sub-levels [19]. Calculations indicate that for $B = 150$ G the largest additional energy gap for allowed optical transitions is of about ± 380 MHz. The overall width for the Zeeman profile of the 834.72 nm transition would then be around 2 GHz, i.e. 1700 m s^{-1} in terms of velocity spread, owing to convolution between all Zeeman lines. All aforementioned effects cannot explain the shape of the observed line profiles and changes in the course of the ion flow although they influence the spectral width, especially the Zeeman effect in the area of a strong magnetic field. Nonetheless, in this contribution any deconvolution procedure is applied and the measured fluorescence profile is assumed to image the local Xe^+ ion VDF.

A series of raw Xe^+ ion axial VDFs are shown in figure 4. All VDFs were measured along the channel axis of the PPS®X000 thruster operating at 500 V. As can be seen, the SNR is relatively high. The combination of a single-mode optical fiber with appropriate collimation optics allows one to control laser energy deposition into the measurement volume, hence, a gain in the fluorescence yield. The SNR is the dimensionless ratio of the signal power to the noise power, $\mathrm{SNR} = (A_{signal}/A_{noise})^2$, where A is the rms amplitude. In this study, one typically finds SNR ≈ 6 that permits one to observe fine details on the ion VDF. In contrast to previous studies [15], the VDFs are smoothed with the classical averaging method in order to determine macroscopic quantities. A statistical analysis of several measurement series gives the experimental error bars: $\pm 5\%$ for the mean velocity and $\pm 15\%$ for the

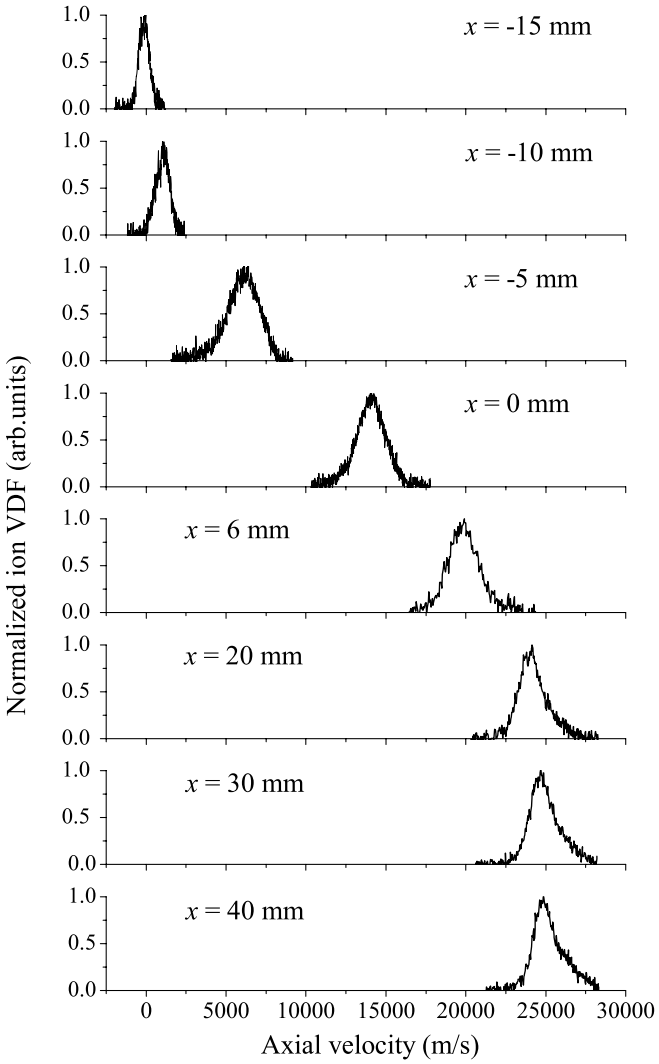

Figure 4. Normalized Xe^+ ion VDFs measured by means of LIF spectroscopy along the channel centerline of the PPS®X000 Hall thruster operating at 500 V. The position $x = 0$ mm corresponds to the exit plane.

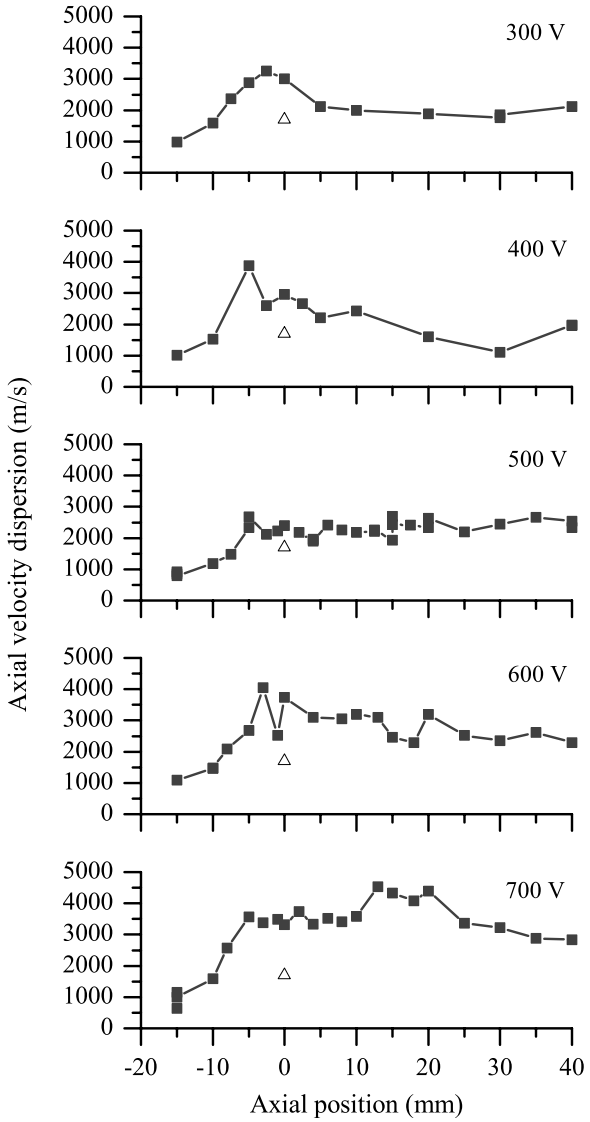

Figure 5. Development of the Xe^+ ion axial velocity dispersion p along the thruster channel axis for various values of the applied voltage U_d. The triangle symbol corresponds to the estimated Zeeman width due to the magnetic field (150 G).

velocity dispersion, respectively. As can be seen in figure 4, the shape of the ion VDF changes when moving downstream. The distribution broadens in the course of the ion flow. A slow wing appears inside the channel whereas a fast wing is visible at the end of the acceleration region. Those points are examined in detail in the rest of the paper.

Instead of comparing time-averaged ion VDF with one another, it is much wiser to analyze statistical quantities directly inferred from the moments of the VDF:

- The mean ion axial velocity $\overline{v}_x$ is obtained from the first-order moment of the velocity distribution.
- The velocity spread or dispersion σ corresponds to the standard deviation; it is computed from the second-order moment of the distribution.
- The so-called maximum ion velocity v_{max} corresponds to the velocity for which the amplitude of the distribution drops down to 10% of its maximum value on the high velocity side [10]. The arbitrary 10% factor is chosen for two reasons, namely (i) it permits an unambiguous definition of v_{max} as the true maximum velocity is difficult to determine and (ii) the fraction of ions moving with the v_{max} velocity is significant.
- The p parameter is another way to define the velocity dispersion. It reads

$$p = 2\sqrt{2\,\mathrm{Ln}(2)} \times \sigma \approx 2.335 \times \sigma, \qquad (1)$$

where σ is the standard deviation. The quantity p is equal to the FWHM in the case of a Gaussian distribution. In the rest of the paper the p parameter is used as a value of the dispersion.

The most probable velocity is not used here. However, its value is close to the mean velocity.

3. Interconnection between ionization and acceleration layers

The Xe^+ ion VDF broadens along the x direction as can clearly be seen in figure 4. The evolution of the VDF width p with the voltage U_d is shown in figure 5. The dispersion follows a single-peaked curve whatever the magnitude of U_d. The maximum value of p, which is around 4000 m s^{-1}, is reached in the vicinity of the thruster channel exit plane. The fact that the widest ion VDF are encountered at the channel exhaust is not related to the magnetic field distribution, though the latter may have an impact. Besides, as measurements are performed along the channel centerline, the divergence has no impact on the velocity dispersion [16]. The large value of p originates from the interconnection between the ionization and the acceleration regions, as explained hereinafter. In contrast to what was reported before [15], the dispersion profile does not really reach a plateau above 500 V. Nevertheless, the position at which p is the highest is shifted downstream when the voltage rises. The applied voltage also has a strong influence upon the value of the velocity dispersion. The maximum dispersion increases with U_d from 3250 m s^{-1} at 300 V up to 4500 m s^{-1} at 700 V. The impact of U_d is even more obvious when considering the spread in kinetic energy ΔE_k. Whereas ΔE_k is around 25 eV at 300 V, it reaches 156 eV at 700 V, i.e. 22% of the applied potential energy. The anode flow rate and the magnetic field do not influence much the velocity dispersion profile [15]. The on-axis development of the p parameter at $U_d = 300$ V and $\Phi_a = 6$ mg s^{-1} is displayed in figure 5. At $\Phi_a = 15$ mg s^{-1}, the highest value of the dispersion is equal to 2600 m s^{-1}; it is reached at $x \approx -5$ mm. At the end of the acceleration region, the dispersion is 1800 m s^{-1}. A large value of the Xe^+ axial velocity dispersion was also observed in the PPS100 thruster [10]. The maximum value of p was of about 4000 m s^{-1}. The behavior as a function of the input voltage U_d is identical.

The broadening of the Xe^+ ion VDF in the course of the flow and the value of the velocity dispersion are at present well understood. They originate in the overlapping between the ionization and the acceleration layers [10, 15]. The broadening of the Xe^+ ion VDF along the channel axis in the direction of the flow is a general feature for HETs that does depend neither on the size of the thruster nor on the operating conditions. Numerical simulations carried out with both a hybrid model [20] and a Particle-in-Cell (PIC) model [6] show that the ion VDF broadening phenomenon finds its origin in the existence of a partial overlap between the ionization layer and the acceleration layer. Calculations carried out with a hybrid model when the electron properties are frozen indicate that the on-axis distribution of the velocity dispersion p depends strongly on both the shape and the position of the ion source term [21]. These two parameters in fact determine the degree of overlap between the two zones. Oscillations of the accelerating potential can amplify the phenomenon when they lead to an increase in the length of the overlap region. Charge exchange collisions between Xe atoms and Xe^+ ions play a minor role in the value of p as the mean free path length (∼30 cm near the exit plane) is far above the typical size of the acceleration layer (∼2–3 cm) [10]. Computational simulations also indicate that the maximum of the velocity dispersion is reached at the end of the ionization layer. Experimental results displayed in figure 5 can therefore be interpreted as follows. The dispersion increases and the maximum value of p is shifted downstream when U_d is ramped up as the overlap between the ionization and acceleration zones increases with the voltage. Such properties are likely linked to the electron temperature that rises with the applied voltage [22, 23]. Ionization is favored along the electron trajectories at high voltage, hence the ion source term extends over the region of the large magnetic field.

Our works reveal that a large fraction of ions are produced inside the acceleration region. The overlapping between the two regions is at the origin of a strong interrelation between the ionization and acceleration processes. As a consequence, the thrust level and the specific impulse of a single-stage HET cannot be tuned in an independent manner, which limits the versatility of such a propulsion device. The only way to reduce the degree of interrelation is to move to a more advanced two-stage thruster design for which ionization and acceleration processes are physically separated [24].

4. Velocity profile

4.1. On-axis velocity development

The evolution of the Xe^+ ion axial mean $\overline{v}_x$ and the maximum v_{max} velocity as a function of the axial position x is displayed in figure 6 for several values of U_d. In figure 6, the dashed line corresponds to the ion velocity obtained assuming a full conversion of the potential energy $e \cdot U_d$ into axial kinetic energy. The highest value of the mean ion axial velocity component is close to the theoretical limit but it always stays below. The supplied potential energy $e \cdot U_d$ is in fact not fully converted into axial motion: a fraction is transformed into radial motion [13, 16], a part contributes to ionization and a part is used to heat up the electron gas. Moreover, voltage losses at the cathode make anyway the potential available for acceleration below the applied potential. The length of the acceleration layer is around 40 mm, as can be seen in figure 6. The shape of the velocity profile depends on the applied voltage: the gradient is steeper when U_d is ramped up and the whole profile is shifted towards the anode. The impact of the PPS®X000 thruster magnetic field was described in a previous paper [15]. In short, the magnetic field has a little influence on the ion velocity, however, the velocity profile slightly moves upstream when the field magnitude increases. The same tendencies were observed with the PSS100 thruster [10]. The influence of the gas flow rate is addressed in section 5.1.

The maximum ion velocity v_{max} is often above the limit given by U_d, especially at high discharge voltages, as can be observed in figure 6. Therefore, there is a non-negligible fraction of Xe^+ ions that have a kinetic energy greater than the given energy. Such fast ions were as well found in the far-field plasma plume of the PPS100 thruster by means of a RPA [25, 26] and a mass spectrometer [27]. Moreover, they were detected by LIF spectroscopy in the near plume of a 200 W Hall thruster [28]. Mechanisms that are responsible for

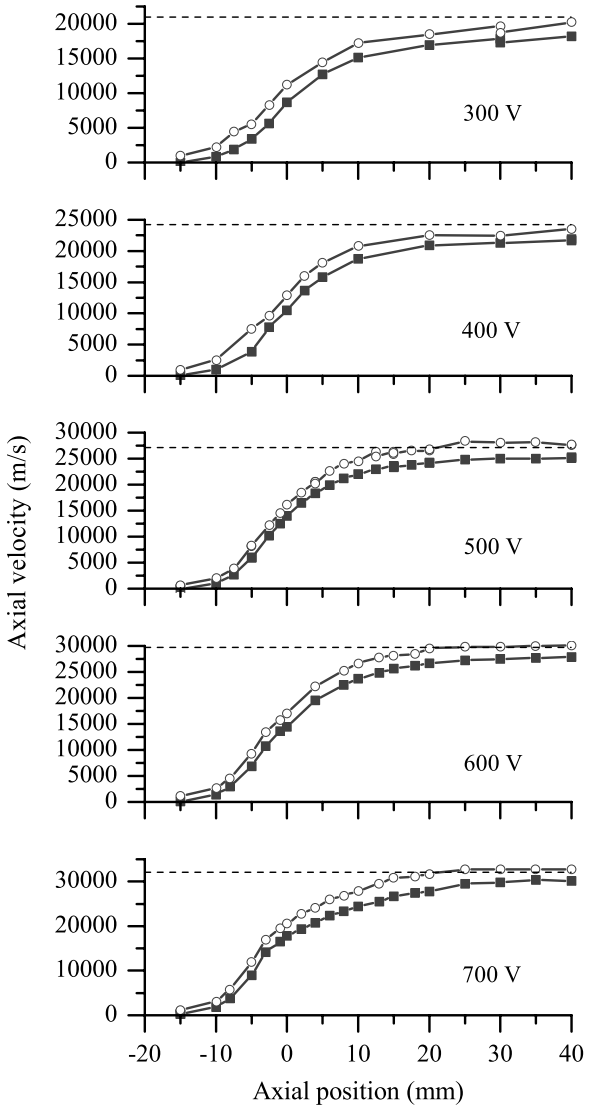

Figure 6. Distribution of the Xe^+ ion axial velocity component along the channel centerline of the PPS®X000 thruster for several values of U_d. The mean velocity $\overline{v}_x$ (square) as well as the maximum velocity v_{max} (circle) are plotted. The dashed line corresponds to the velocity that can be achieved when the potential energy is fully converted into axial motion.

the creation of very fast Xe^+ ions are discussed in section 6.2 in light of recent numerical and experimental outcomes. As a counterpart of fast ions, very slow ions are always observed in the plasma of a HET [10, 15, 28].

4.2. Outcome of hybrid kinetic/fluid modeling

So far, computer simulations performed with a hybrid kinetic/fluid model failed to correctly reproduce the experimental measurements of the space distribution of the Xe^+ ion velocity [20, 29, 30]. The hybrid modeling tool cannot describe self-consistently the anomalous electron transport across the magnetic barrier. The electron mobility perpendicular to the magnetic field lines is then defined by means of two tunable coefficients that represent Bohm-like and wall-enhanced transport [20, 31]. Although simple, such

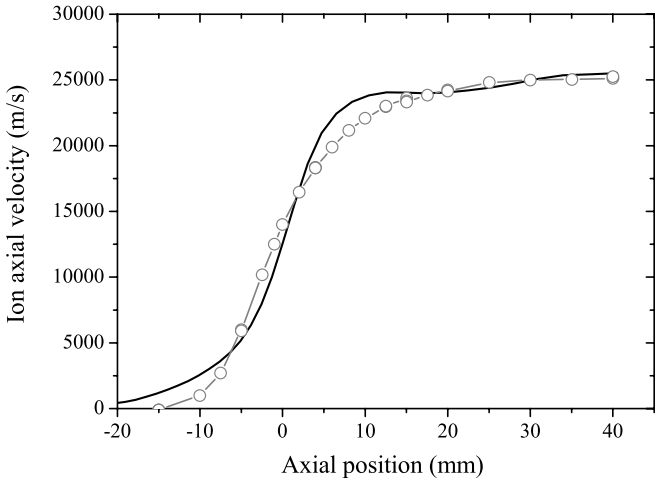

Figure 7. Comparison between the on-axis distribution of the Xe^+ ion mean axial velocity measured by LIF spectroscopy (circle) and computed with a hybrid numerical model (line). The PPS®X000 thruster was fired at 500 V and 6 mg s^{-1}.

a picturing of anomalous transport was sufficient to reproduce many features and properties of a thruster like the current waveform, the fraction of accelerating potential inside and outside the channel, the thrust and the specific impulse level.

A more realistic approach is at present put to the test. Instead of two coefficients, an electron mobility profile is introduced into the hybrid model [32]. Both the shape of the profile and the magnitude of the mobility are chosen in compliance with outcomes of a PIC model [6]. This approach is somehow similar to the one investigated by Cappelli's group in Stanford University, in which they combined a hybrid model and experimental measurements of the electron mobility to simulate Hall thruster plasma properties [33]. In figure 7, the Xe^+ ion axial velocity distribution measured by way of LIF spectroscopy along the channel axis of the PPS®X000 thruster firing at 500 V is compared with the distribution computed with the hybrid modeling tool. The agreement between the two curves is quite satisfactory. The growth rate of the velocity in the channel exhaust region is, however, overestimated by the simulation. The numerical tool was also able to give the proper thrust and current levels. This first attempt is therefore promising and it opens the way to the in-depth investigation of PIC-hybrid model combination true potentiality.

5. Electric field distribution

5.1. Mean electric field profile

The electric field in the axial direction E_x is the derivative of the acceleration potential that corresponds to the potential drop within the acceleration area:

$$|E_x(x)| = \frac{\mathrm{d}U_{acc}(x)}{\mathrm{d}x} = \frac{m}{e}v(x)\frac{\mathrm{d}v(x)}{\mathrm{d}x}. \qquad (2)$$

In order to numerically compute E_x, it is necessary to smooth the potential profile and to interpolate the resulting curve using, e.g. cubic splines. The electric field distribution along the PPS®X000 channel axis is shown in figure 8 for various

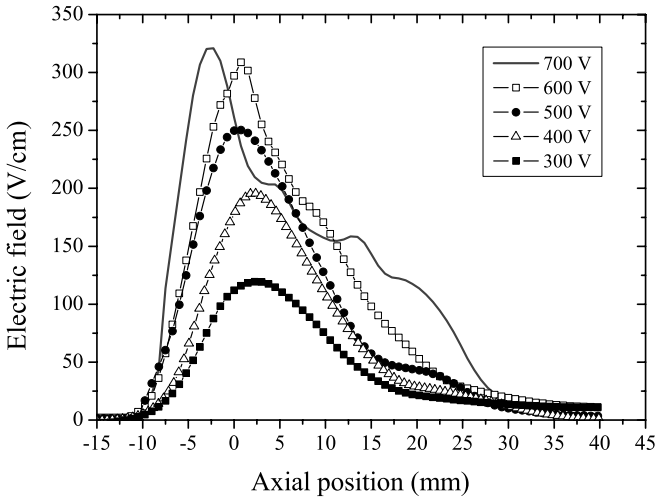

Figure 8. Distribution along the channel centerline of the PPS®X000 thruster axial electric field E_x as a function of the discharge voltage ($\Phi_a = 6\,\mathrm{mg\,s^{-1}}$). The electric field is computed from the mean ion velocity $\overline{v}_x$.

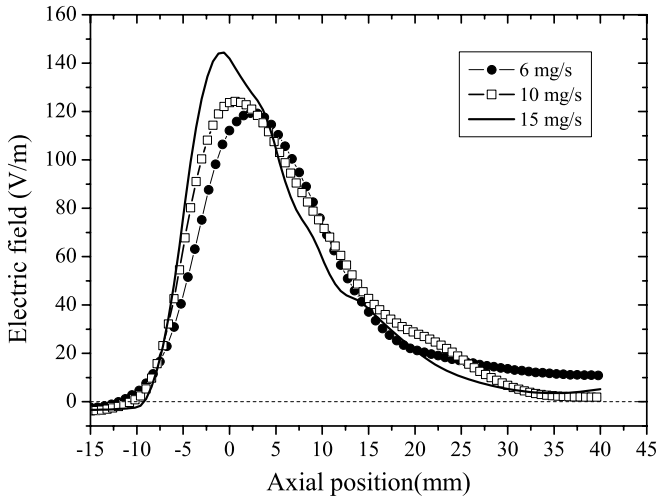

Figure 9. Distribution along the channel centerline of the PPS®X000 thruster axial electric field E_x as a function of the xenon anode mass flow rate ($U_d = 300\,\mathrm{V}$). The electric field is computed from the mean ion velocity $\overline{v}_x$.

voltages and in figure 9 for several propellant mass flow rates. Each curve represents the electric field calculated from the corresponding Xe^+ mean velocity profile.

As shown in figure 8, the magnitude of E_x increases with U_d and the maximum of the field tends to shift upstream when U_d is ramped up. Linnel and co-workers observed identical trends for the high-power 173Mv1 Hall thruster from NASA, though they found a stronger field [23]. A large part of the acceleration region is located outside the channel whatever the voltage, as can be seen in figure 8. This fact becomes obvious when considering the accelerating potential U_{acc}. Table 1 shows the fraction of potential inside the thruster channel ΔU_{in} calculated as follows:

$$\Delta U_{in} = \frac{U_{acc}|_{x=0}}{U_{acc}}, \qquad (3)$$

where U_{acc} is computed from the profile of the mean ion axial velocity. As the electric field moves a little towards the anode when U_d rises, the fraction of accelerating potential inside the channel increases, as shown in table 1. Note that the gap between U_d and U_{acc} stays constant at ∼75 V whatever the value of the discharge voltage. In other words, voltage losses do not depend on U_d. In contrast to what was mentioned in a previous paper [15], the extent of the electric field on-axis distribution, i.e. the length of the acceleration layer, does not change when the discharge voltage increases. The previous conclusion was erroneous due to a wrong choice for the definition of the electric field extent. Table 1 contains the value of the mean electric field $\overline{E}_x$ within the acceleration zone. It increases with U_d as expected from curves in figure 8. A quantity δE_x can be defined to characterize the expansion of the field. Here, the quantity δE_x is the ratio of U_{acc} to $\overline{E}_x$. The value of the length δE_x is ∼4.7 cm whatever the magnitude of the voltage. The same conclusion holds when considering the width (FWHM) of the axial electric field: it stays equal to ∼15.5 mm. The accelerating electric field properties with the applied voltage are found to be different for the PPS100 thruster [10]. Although the field moves towards the anode and its magnitude rises with the discharge voltage, the spatial extent of the field narrows down when U_d increases. The evolution of the electron kinetic energy with the applied voltage could partly explain the measurement outcomes. At high voltage electrons are not efficiently confined as their Larmor radius increases. They penetrate deeper into the magnetic barrier, hence the electric field shifts towards the anode. A precise explanation for the impact of the applied voltage on the acceleration region length remains unclear. Anyhow, a proper description of the electric field properties implies to better grasp anomalous electron transport perpendicular to the magnetic field lines. A last remark is worth making. As the electric field tends to move upstream when the voltage augments, the region within which the ionization and acceleration processes are mixed up is most likely enlarged. As a consequence, the ion velocity dispersion should become greater, as shown in section 3.

The on-axis development of the electric field E_x as a function of the xenon mass flow rate for $U_d = 300\,\mathrm{V}$ is shown in figure 9. Values of the quantities associated with the electric field are presented in table 1. The amplitude of E_x rises when the the mass flow rate mounts whereas the averaged field strength stays unchanged. The length δE_x is equal to ∼4.7 cm whatever the value of Φ_a meaning that the size of the acceleration zone is not affected by a change in the propellant flow. The width (FWHM) of the electric field distribution tends to lower by contrast. As can be seen in figure 9, the electric fields shifts upstream when the flow rate increases. Numbers in table 1 indicate that the fraction of accelerating potential inside the channel increases with the gas flow. Surprisingly, measurements performed during a previous campaign with the same thruster show that the electric field moves downstream when the mass flow rate is ramped up [15]. The HET operating conditions were $U_d = 500\,\mathrm{V}$, $\Phi_a = 6$ and $9\,\mathrm{mg\,s^{-1}}$. It therefore seems that the effect of the mass flow rate on the electric field properties cannot be investigated without considering the voltage.

Table 1. Accelerating potential U_{acc}, fraction of the potential inside the channel ΔU_{in} and averaged axial electric field $\overline{E}_x$ for various operating conditions of the PPS®X000 Hall thruster. All quantities are obtained from the Xe^+ ion mean velocity profile.

Change of U_d ($\phi_a = 6$ mg s^{-1})				Change of Φ_a ($U_d = 300$ V)			
U_d (V)	U_{acc} (V)	ΔU_{in}	$\overline{E}_x$ (V cm^{-1})	Φ_a (mg s^{-1})	U_{acc} (V)	ΔU_{in}	$\overline{E}_x$ (V cm^{-1})
300	225	0.23	48	6	225	0.23	48
400	323	0.23	69	10	232	0.27	49
500	432	0.31	94	15	231	0.33	48
600	530	0.27	111				
700	622	0.35	132				

5.2. Data analysis using the Boltzmann's equation

As a non-negligible amount of Xe^+ ions are created within the acceleration layer, see section 3, the accelerating potential computed from the mean velocity profile is underestimated [15]. The use of v_{max} instead of $\overline{v}$ could provide a more realistic value of the local potential as the fastest ions necessarily experience the full potential drop. However, a large number of fast ions have a kinetic energy above the potential energy $e \cdot U_d$. Thus, when using v_{max}, the local potential is overestimated. A correct estimate of the time-averaged potential profile is not straightforward, as it strongly depends upon processes accounted for.

A novel and powerful method has recently been developed for evaluating the true spatial profile of the electric field as well as the distribution of the ionization frequency f_i [34]. The ionization frequency represents the number of electron–ion pair creation per unit time and per electron. The ionization rate S_i is linked to f_i by way of the formula $S_i = f_i \cdot n_e$, where n_e is the plasma density. The ionization frequency can be assessed by measuring the electron parameters n_e and T_e as well as the gas density. The novel approach consists of establishing a relationship between the two quantities of interest and the moments of the measured ion VDFs through the Boltzmann's equation. Note that to obtain proper results, the experimental VDFs must be normalized taking into account the laser power, the detector response and the lock-in amplifier settings. The electric field as well as the ionization frequency profiles along the channel axis obtained from the moments of the ion VDFs recorded at $U_d = 600$ V are shown in figure 10. The computed distribution of E_x is similar to the one inferred from the mean axial velocity profile. There is a large overlap between the electric field and the ionization profiles, which indicates that a part of the ionization process occurs in a region of the strong electric field. Figure 11 shows the accelerating electric field spatial profile as a function of the thruster discharge voltage obtained when the method based on the ion VDF moments is employed. The electric field distributions are close to the ones shown in figure 8. Similar conclusions hold; however, sliding of the electric field profile towards the anode is less clear. As the ionization process is accounted for in the method, the effect of ions created at the beginning of the acceleration layer is withdrawn. Ions accelerated to speed above the theoretical limit are, conversely, included. Nonetheless, in the region of interest such ions originate from oscillations of the electric field, as we will see. Thus, they naturally contribute to the time-averaged electric field distribution.

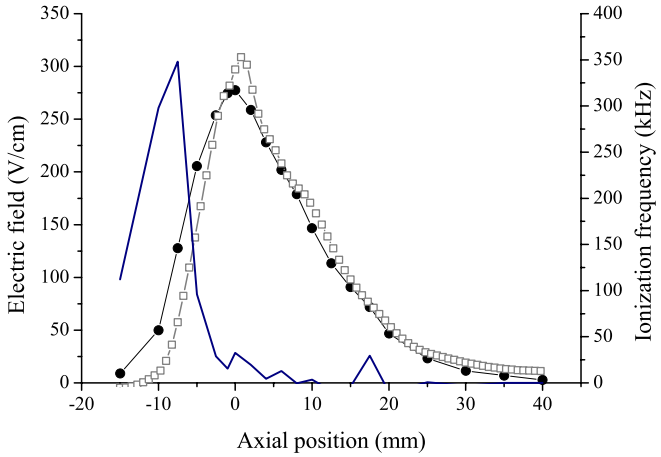

Figure 10. On-axis electric field development at $U_d = 600$ V and $\phi_a = 6$ mg s^{-1} resulting from two approaches: measurement of the Xe^+ ion mean velocity (square) and calculation of the ion VDF moments (circle). Also shown is the ionization frequency profile determined from the second method.

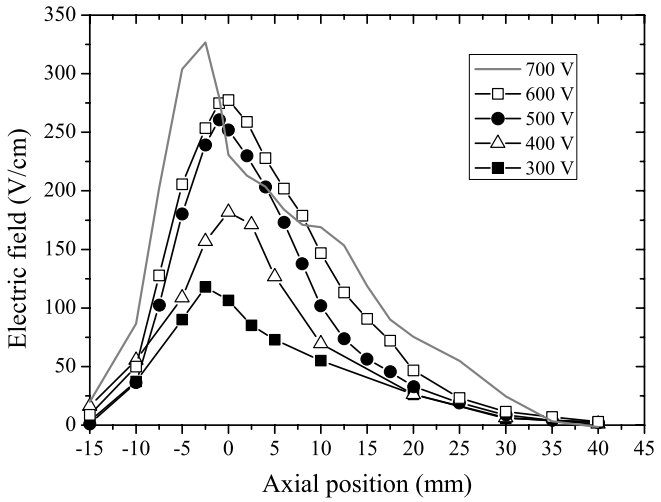

Figure 11. Plots of the electric field distribution along the channel centerline for several discharge voltages. Curves originate from a method based on the moments of the ion VDFs.

6. RPA diagnostics

6.1. Measuring device and RPA traces

The ion current incident on a RPA located on the PPS®X000 thruster centerline 70 cm away from the thruster exit plane was recorded as a function of ion axial energy by varying the

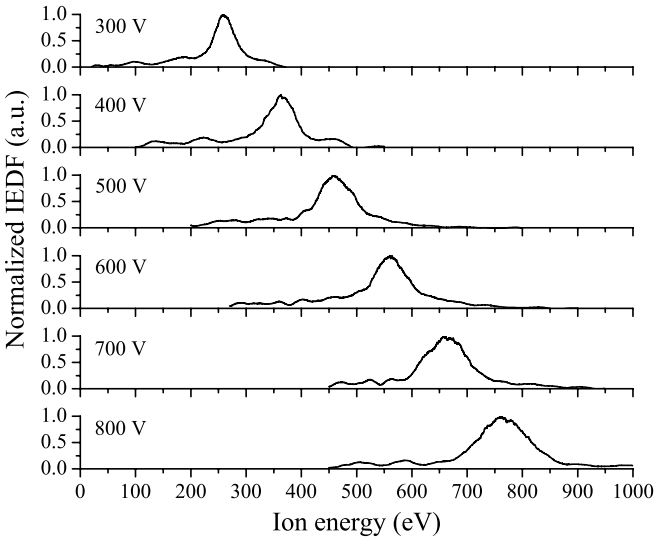

Figure 12. Ion energy distribution curves measured by means of a RPA for various voltages. The RPA is located on the PPS®X000 thruster axis 70 cm away from the exit plane.

repelling potential on the analyzing grid [9]. The far-field ion VDF is then inferred from the numerical derivative of the $I(V)$ trace. The current measurement of a RPA is not dependent on the ion energy, but rather on the energy per unit charge. Thus a RPA cannot distinguish between singly and multiply charged ions. The RPA employed here is composed of four stainless steel grids with 0.2 mm holes with a 1.5 mm gap in between one another and a copper collector. The first grid is at floating potential V_f. The latter is then the reference point. The second grid is negatively polarized (−10 V) with respect to V_f to repel electrons. The third grid has a variable positive potential applied to it; it acts as a high-pass filter for ions. The last grid is biased negative (−4 V) to prevent secondary electrons emitted by the collector from escaping. The design of the RPA is especially suited for operation at high voltage, up to 1000 V. The grid mounts are optimized to avoid short-circuit due to grid material sputtering. A ceramic tube 40 mm in length with a sampling orifice 7 mm in diameter was mounted ahead of the RPA first grid to produce a collimated ion beam as well as to limit the ion flow entering the device.

The recorded ion energy distribution functions (EDFs) are displayed in figure 12 for several discharge voltages. The mean ion energy in the far field is close to the overall accelerating potential measured by means of LIF spectroscopy, the gap being below 10 eV. The ion EDF stretches out when the voltage is ramped up. The width (FWHM) of the RPA curves ranges from 45 eV at 300 V up to 106 eV at 800 V. A low-energy tail of ions was found in all RPA traces, see figure 12. A high-energy tail of ions with kinetic energy well above the discharge voltage is also found in all traces. As can be seen in figure 12, the fraction of very fast ions, referred to as supra-sped up ions, is significant. The origin of slow ions is well identified. In the acceleration layer they result from the ionization process [10]. In the plasma plume near and far field, they are produced by charge exchange collisions that arise from the interaction between the ion flow and the background gas [25, 27]. The origin of very fast ions is still debated; however, recent advances bring a new perspective.

Table 2. Fraction in percent of supra-sped up ions Λ obtained by means of LIF spectroscopy ($x = 40$ mm) and RPA ($x = 70$ cm), see equation (4).

Voltage (V)	LIF	RPA
300	<3.0	8.6
400	3.0	10.7
500	6.4	15.6
600	5.3	16.1
700	9.7	16.8
800	—	20.9

6.2. *Supra-sped up ions*

The evolution of the fraction of supra-sped up ions Λ as a function of the discharge voltage is reported in table 2. The limit in terms of kinetic energy E_k is arbitrarily taken to be the applied potential energy $e \cdot U_d$. This fraction then reads

$$\Lambda = \frac{\int_{e \cdot U_d}^{\infty} f(E_k)\,\mathrm{d}E_k}{\int_0^{\infty} f(E_k)\,\mathrm{d}E_k}, \qquad (4)$$

where f is the EDF measured either by LIF spectroscopy at $x = 40$ mm or by RPA at $x = 700$ mm. Table 2 indicates that the fraction Λ increases with the discharge voltage. Furthermore, at a given voltage, the fraction is always larger in the plume far field. It shows that very fast ions are continuously produced in the course of the ion flow. Charge-exchange collisions and momentum transfer processes between atom and/or Xe^+ ions and multiply charged ions like Xe^{2+} and Xe^{3+} can possibly explain the production of supra-sped up Xe^+ ions in the plasma of a Hall thruster. These two types of processes may be responsible for the large fraction of fast ions recorded far away from the channel exhaust as they are solely efficient over long distances in a rarefied environment. Moreover, the fraction of multiply charged ion species increases with U_d in compliance with numbers given in table 2. Nevertheless, the aforementioned mechanisms can hardly explain the existence of fast ions at the end of the acceleration layer with energy close to the discharge energy. Another mechanism must then be put forward.

Xe^+ ions can also acquire a very large speed due to oscillations of the electric field in space and in time. Computer simulations carried out with a hybrid model suggest that oscillations of the electric field are at the origin of the production of very slow ions and supra-sped up ions [31]. PIC simulations predict as well the existence of very fast and very slow ions whereas the charge transfer process and multiply charged ions are not included into the model [6, 10]. Recent calculations carried out by our team confirm this assumption. A kinetic model with a fixed ionization region and a constant source term unambiguously show that oscillations in time of the electric field with frequencies that correspond to the reciprocal of the Xe^+ ion transit time across the acceleration layer ($f \approx 100$–500 kHz) generate fast and slow Xe^+ ions, the average kinetic energy of the ion fluid always staying below

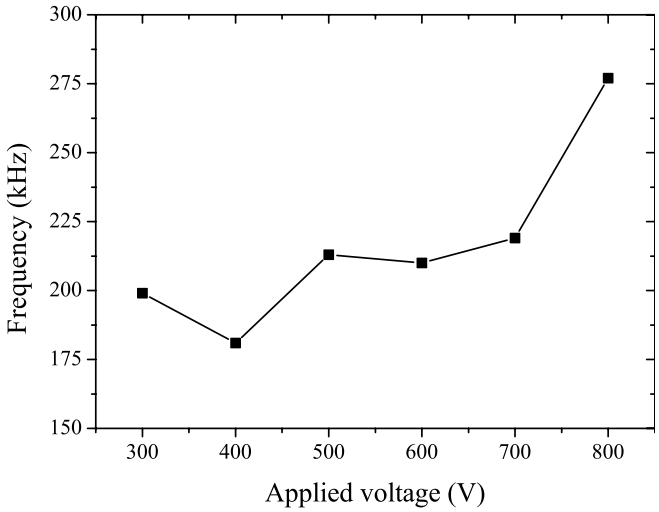

Figure 13. Averaged frequency of plasma oscillations in the range 100–500 kHz as a function of U_d. Signals were recorded with a Langmuir probe at the channel exhaust.

the given potential energy. The two specific kind of ions are in fact generated by way of a wave-riding mechanism that occurs when ion motion and field oscillations are synchronized [10]. Furthermore, all kinds of numerical simulations show that the fraction of supra-sped up ions rises with the frequency and the amplitude of the electric field fluctuations.

6.3. Plasma oscillations at the ion transit time scale

Oscillations of the PPS®X000 thruster plasma have been recorded by means of an unbiased shielded low-impedance cylindrical Langmuir probe in the region of strong electric and magnetic fields. The tungsten probe tip 3 mm in length and 0.1 mm in diameter is located in the channel exit plane at the ion beam boundary. Besides, the probe is parallel to the magnetic field lines. The probe is in fact inserted through the slit used for LIF experiments, see section 2.1. Signals captured by the probe are transferred by means of a 50 Ω transmission line equipped with a 50 Ω vacuum feedthrough to a 1 GHz bandwidth digital oscilloscope. The discharge current signal is used as a trigger to synchronize waveform acquisition. Signals were acquired over a 1 MΩ load in dc and ac modes. The probe design combined with the measurement procedure warrants that plasma potential fluctuations are monitored [35]. A recorded time-series consists of the ensemble average over 128 acquisitions. The empirical mode decomposition technique is used to separate the low-frequency part (3–50 kHz) and the mid-frequency part (100–500 kHz) of the measured probe waveforms [36]. The high-frequency part of the signal is ignored. Low-frequency oscillations mostly correspond to the so-called plasma breathing mode that finds its origin in a prey–predator type process between atoms and ions inside the channel [37]. Mid-frequency plasma fluctuations certainly correspond to the ion transit time oscillations of which the origin is still unclear [37, 38].

Figure 13 shows the evolution of the averaged frequency of the mid-frequency component of the plasma oscillations as a function of the discharge voltage. It is clear that the frequency increases with the voltage. Potential fluctuations recorded by means of an unbiased probe within a given frequency range image oscillations of the thruster electric field in the same frequency interval. In summary, the series of experiments carried out in this study show up two facts. First, the fraction of supra-sped up ions grows when the applied voltage is ramped up. Second, the electric field oscillation frequency at the ion transit time scale augments with the voltage. These experimental facts suggest the existence of a relation between the production of very fast ions and oscillations of the electric field.

7. Conclusion

The time-averaged VDFs of Xe^+ ions along the channel centerline of the high-power PPS®X000 Hall thruster have been measured by means of near-infrared continuous-wave LIF spectroscopy for several operating conditions. The discharge voltage was varied from 300 up to 700 V keeping the gas flow unchanged at 6 mg s^{-1}. The xenon mass flow rate was changed from 6 to 15 mg s^{-1} with an applied voltage of 300 V. In the two cases the magnetic field strength is kept fixed. From the recorded ion VDFs, statistical quantities such as the mean axial velocity and the velocity dispersion were calculated.

The profile of the velocity dispersion can be interpreted in terms of overlapping between the ionization and the acceleration zones. This phenomenon is found to increase with the discharge voltage. The interrelation between the two regions is a general feature of single-stage HETs, which limits such propulsion devices in terms of flexibility. The experimental on-axis distribution of the ion velocity is in accordance with hybrid kinetic/fluid numerical simulation outcomes for which the electron mobility is given by PIC calculations. The mean ion velocity profile permits the determination of the effective electric field. The latter grows and shifts towards the anode when the voltage is ramped up. The effect of the propellant flow upon the electric field properties is unclear as opposite trends are found depending on the voltage. In all cases, however, most of the acceleration process takes place outside the thruster channel. Due to the creation of ions within the acceleration region, the electric field is underestimated when the mean ion velocity is used. Here, a novel approach based on the moments of the experimental VDF in combination with the Boltzmann's equation is introduced in order to properly assess the electric field distribution. The method also provides the ionization frequency profile, thereby giving evidence for the interconnection between ionization and acceleration processes. Finally, the LIF diagnostics reveals the existence at the end of the acceleration layer of fast ions of which the kinetic energy is above the potential energy. The fraction of these supra-sped up ions augments when the voltage increases.

The ion VDFs were also recorded in the plume far field by way of a RPA for various discharge voltages. A low-energy tail as well as a high-energy tail are visible on all RPA traces. Slow ions originate in Xe–Xe^+ charge-exchange collisions. The origin of very fast ions is less straightforward. In the plasma plume, they likely result from charge exchange and momentum

transfer processes in collision events that involve multiply charged ion species. By contrast, measurements of the plasma potential oscillations, together with computer simulations, suggest that, in the region of a strong electric field, supra-sped up ions may find their origin in spatial and temporal oscillations of the electric field in the frequency range associated with the so-called ion transit time instability. Nevertheless, other dedicated experimental studies are necessary to definitely establish this assumption.

Acknowledgments

The authors would like to acknowledge fruitful discussions with Dr N Sadeghi from the Laboratoire de Spectrométrie Physique in Grenoble. The authors also thank Dr P Lasgorceix for designing the HV version of the RPA. Works are performed in the framework of the joint research programme CNRS/CNES/SNECMA/Universities 3161 entitled '*Propulsion par plasma dans l'espace*'. They are also financially supported by the French National Research Agency in the framework of the 06-BLAN-0171 *TELIOPEH* project.

References

[1] Frisbee R H 2003 *J. Propulsion Power* **19** 1129
[2] Zhurin V V, Kaufmann H R and Robinson R S 1999 *Plasma Sources Sci. Technol.* **8** R1
[3] Morozov A I and Savelyev V V 2000 Fundamentals of stationary plasma thruster theory *Reviews of Plasma Physics* vol 21 ed B B Kadomtsev and V D Shafranov (New York: Consultant Bureau) p 203 and references therein
[4] Kim V 1998 *J. Propulsion Power* **14** 736
[5] Janes G S and Lowder R S 1966 *Phys. Fluids* **9** 1115
[6] Adam J C, Héron A and Laval G 2004 *Phys. Plasmas* **11** 295
[7] Koo J W and Boyd I D 2006 *Phys. Plasmas* **13** 033501
[8] Gascon N, Dudeck M and Barral S 2003 *Phys. Plasmas* **10** 4123
[9] Ahedo E and De Pablo V 2007 *Phys. Plasmas* **14** 083501
[10] Gawron D, Mazouffre S, Sadeghi N and Héron A 2008 *Plasma Sources Sci. Technol.* **17** 025001
[11] Mazouffre S, Pérez Luna J and Dannenmayer K 2007 *J. Appl. Phys.* **102** 023304
[12] Hargus W A Jr and Cappelli M A 2001 *Appl. Phys.* B **72** 961
[13] Hargus W A Jr and Charles C S 2008 *J. Propulsion Power* **24** 127
[14] Dorval N, Bonnet J, Marque J P, Rosencher E, Chable S, Rogier F and Lasgorceix P 2002 *J. Appl. Phys* **91** 4811
[15] Mazouffre S, Gawron D, Kulaev V and Sadeghi N 2008 *IEEE Trans. Plasma Sci.* **36** 1967
[16] Hargus W A Jr and Cappelli M A 2002 *J. Propulsion Power* **18** 159
[17] Hargus W A Jr and Nakles M R 2008 *IEEE Trans. Plasma Sci.* **36** 1989
[18] Demtröder W 1998 *Laser Spectroscopy* (New York: Springer)
[19] Hollas J M 1998 *High Resolution Spectroscopy* (New York: Wiley)
[20] Bareilles J, Hagelaar G J M, Garrigues L, Boniface C, Boeuf J P and Gascon N 2004 *Phys. Plasmas* **11** 3035
[21] Mazouffre S, Gawron D, Kulaev V, Pérez Luna J and Sadeghi N 2008 *AIP Conf. Proc.* vol 993 ed H J Hartfuss *et al* (New York: AIP) p 447
[22] Raitses Y, Staack D, Keidar M and Fisch N J 2005 *Phys. Plasmas* **12** 057104
[23] Linnell J A and Gallimore A D 2006 *Phys. Plasmas* **13** 103504
[24] Mazouffre S *et al* 2008 *Proc. 5th International Spacecraft Propulsion Conference (Heraklion, Crete, Greece)* paper 42-068
[25] King L B, Gallimore A D and Marrese C M 1998 *J. Propulsion Power* **14** 327
[26] Gawron D, Mazouffre S, Albarède L and Sadeghi N 2006 *Proc. 42nd AIAA/ASME/SAE/ASEE Joint Propulsion Conf. (Sacramento, CA)* AIAA paper 06-4473
[27] King L B and Gallimore A D 2004 *J. Propulsion Power* **20** 228
[28] Hargus W A Jr and Nakles M R 2006 *Proc. 42nd AIAA/ASME/SAE/ASEE Joint Propulsion Conf. (Sacramento, CA)* AIAA paper 06-4991
[29] Hagelaar G J M, Bareilles J, Garrigues L and Boeuf J P 2002 *J. Appl. Phys.* **91** 5592
[30] Pérez Luna J, Hagelaar G J M, Garrigues L and Boeuf J P 2007 *Phys. Plasmas* **14** 113502
[31] Hagelaar G J M, Bareilles J, Garrigues L and Boeuf J P 2003 *J. Appl. Phys.* **93** 67
[32] Adam J C *et al* 2008 *Plasma Phys. Control. Fusion* **50** 124041
[33] Scharfe M K, Gascon N, Cappelli M A and Fernandez E 2006 *Phys. Plasmas* **13** 083505
[34] Pérez-Luna J, Hagelaar G J M, Garrigues L and Boeuf J P 2009 *Plasma Sources Sci. Technol.* at press
[35] Lazurenko A, Albarède L and Bouchoule A 2006 *Phys. Plasmas* **13** 083503
[36] Kurzyna J, Mazouffre S, Lazurenko A, Albarède L, Bonhomme G, Makowski K, Dudeck M and Peradzyński Z 2005 *Phys. Plasmas* **12** 123506
[37] Choueiri E Y 2001 *Phys. Plasmas* **8** 1411
[38] Barral S, Makowski K, Peradzyński Z and Dudeck M 2005 *Phys. Plasmas* **12** 073504